Channel flow of rigid sphere suspensions: Particle dynamics in the inertial regime

Iman Lashgari [a,*], Francesco Picano [a,b], Wim Paul Breugem [c], Luca Brandt [a]

[a] Linné Flow Centre and SeRC (Swedish e-Science Research Centre), KTH Mechanics, S-100 44 Stockholm, Sweden
[b] Industrial Engineering Department, University of Padova, Padova, Italy
[c] Laboratory for Aero & Hydrodynamics, TU-Delft, Delft, The Netherlands

ARTICLE INFO

ABSTRACT

We consider suspensions of neutrally-buoyant finite-size rigid spherical particles in channel flow and investigate the relation between the particle dynamics and the mean bulk behavior of the mixture for Reynolds numbers $500 \leq Re \leq 5000$ and particle volume fraction $0 \leq \Phi \leq 0.3$, via fully resolved numerical simulations. Analysis of the momentum balance reveals the existence of three different regimes: laminar, turbulent and inertial shear-thickening depending on which of the stress terms, viscous, Reynolds or particle stress, is the major responsible for the momentum transfer across the channel. We show that both Reynolds and particle stress dominated flows fall into the Bagnoldian inertial regime and that the Bagnold number can predict the bulk behavior although this is due to two distinct physical mechanisms. A turbulent flow is characterized by larger particle dispersion and a more uniform particle distribution, whereas the particulate-dominated flows is associated with a significant particle migration towards the channel center where the flow is smooth laminar-like and dispersion low. Interestingly, the collision kernel shows similar values in the different regimes, although the relative particle velocity and clustering clearly vary with inertia and particle concentration.

Introduction

Particles suspended in a carrier fluid can be found in many biological, geophysical and industrial flows. Some obvious examples are the blood flow in the human body, pyroclastic flows from volcanos, sedimentations in sea beds, fluidized beds and slurry flows. Moreover, the knowledge of the particle dynamics is relevant, among others, in biomechanical applications for extracorporeal devices and formation of clots. Suspensions are typically employed to transport and mix particles by means of a carrier fluid (Eckstein et al., 1977). The overall effect of particles on the flow dynamics has therefore a significant impact on the energy consumption of biological and industrial processes. Despite the numerous applications, however, it is still difficult to estimate the force needed to drive suspensions and the internal dissipation mechanisms are not fully understood, especially in a turbulent flow. Unlike single phase flows where the pressure drop can be accurately predicted as a function of the Reynolds number and the properties of the wall surface (roughness effects), additional parameters become relevant in the presence of a suspended phase when the properties of the particles (size, shape, density, stiffness, volume fraction, and mass fraction) affect the overall dynamics of the suspension. The behavior of these multiphase flows becomes even more complicated when the particle volume fraction is high, inertial effects are non-negligible and particles have finite size, i.e. size of the order of the relevant flow structures (Campbell, 1990).

In this study we focus on non-colloidal suspensions, mixtures where the dispersed particles are greater than colloidal in size and thermal fluctuations are negligible. As Brownian motion is negligible there is no diffusion to create an equilibrium structure making the problem one of fundamental non-equilibrium physics. The aim of this study is to gain physical understanding of the role of the fluctuations induced by the suspended phase and their coupling to the mean flow, the effect of particle inertia and the modifications of the particle interactions when increasing the (bulk flow) Reynolds number. As shown also here, it is fundamental to examine the local particle concentration, migration and segregation for a full comprehension of the transport processes at work. Inhomogeneities in the particle distribution are documented at low and finite Reynolds numbers, e.g. the so-called Segre–Silberberg effect (Segré and Silberberg, 1961). Here we document how the interactions between the turbulent flow structures and particle-induced disturbances alter the macroscopic flow behavior.

* Corresponding author. Tel.: +46 760833694.
  E-mail address: imanl@mech.kth.se (I. Lashgari).

Only a few studies have been devoted to the inertial flow of suspensions in the presence of finite size particles. Matas et al. (2003) performed experiments with a suspension of neutrally buoyant particles in pipe flow and defined the laminar and turbulent regimes according to the spectra of the pressure fluctuations between the inlet and exit of the pipe. The critical Reynolds number separating the existence of the two regimes exhibits a non-monotonic behavior with the volume fractions for large enough particles. This result is partially reproduced by the numerical simulations in Yu et al. (2013). Since velocity fluctuations exist at all Reynolds numbers, these authors choose the streamwise velocity perturbation kinetic energy as the criterion to distinguish between laminar and turbulent flow. A more detailed study on the transition of finite-size particle suspensions is performed by Loisel et al. (2013) for a fixed volume fraction of about 5%. The observed reduction of the critical Reynolds number is explained by the breakdown of the coherent flow structures to smaller and more energetic eddies, which prevents the flow relaminarization when decreasing the Reynolds number. The characteristics of a fully turbulent channel flow laden with finite-size particles are presented in Picano et al. (2015), such as the decrease in the Von Karman constant with increasing volume fraction and the increase in the overall drag.

The present work extends the analysis of Lashgari et al. (2014) on the inertial flow of suspensions of finite-size neutrally buoyant spherical particles. In this previous study, we document the existence of three different regimes when varying Reynolds number, Re, and particle volume fraction, Φ. A laminar-like regime where viscous stress exhibits the strongest contribution to the total stress, a turbulent-like regime where the turbulent Reynolds stress mainly determines the momentum transfer across the channel (see also Picano et al., 2015) and a third regime, denoted as inertial shear-thickening, characterized by a significant enhancement of the wall shear stress that is not due to an increment of the Reynolds stress but due to the strong contribution of the particle stress. In the present work, we move our attention from the bulk flow behavior to the local behavior by studying in detail the particle dynamics, single and pair particle statistics. In particular, we examine the particle local volume fraction, dispersion coefficients and collision kernels for the three regimes introduced in Lashgari et al. (2014). Our dataset is based on fully resolved numerical simulations of the two-phase system.

We aim to connect our results to the seminal work by Bagnold (1954). Using experimental data of a suspension of neutrally buoyant solid particles in an annular domain between two concentric cylinders, Bagnold understood that the shearing of closely spaced particles would generate a normal or dispersive stress in addition to the shear stress (Hunt et al., 2002). He used the ratio between the grain inertia and the viscous stress to define different flow regimes. The viscous and inertial regimes introduced by Bagnold are characterized by a linear and quadratic relation between the wall shear/normal stress and the shear rate, respectively. Inspired by Bagnold's experiment, Fall et al. (2010) performed a similar study in plane Couette flow; these authors show a smooth transition from the Newtonian (viscous) to the Bagnoldian (inertial) regime by increasing the shear-rate. The laminar flow at high volume fractions behaves similarly to dry granular flows (Campbell, 1990): the flow experiences discontinuous shear-thickening and fast particle migration toward the regions of low shear. Both effects (shear-thickening and particle migration towards region with low shear) have been observed in several previous investigations of dense suspensions at low Reynolds number, see Hampton et al. (1997), Brown and Jaeger (2009) and Yeo and Maxey (2011) among others. Shear-thickening at higher volume fractions is examined among others in Haddadi and Morris (2014) who clearly identify the role of friction among particles in relative motion. The origin of shear-thickening at lower volume fractions and in the presence of non-negligible inertia is attributed to an additional excluded volume, i.e., the shadow region behind each particle where it

is very unlikely to find a second particle, see Picano et al. (2013). The effective volume fraction of the suspension increases because of the shadow region (a region with statistically vanishing relative particle flux) around the particles. Particle migration across the channel is not an inertial effect and is observed also in Stokes flow at high volume fractions (Yeo and Maxey, 2011). The particles tend to migrate from regions of high to low shear due to the imbalance of the normal stress resulting from the particle interactions (Guazzelli and Morris, 2011).

Less is known of the inertial Bagnoldian regime. It is worth mentioning that, for the same bulk behavior, the Bagnoldian regime can be either Reynolds stress or particle stress dominated, as deduced from the data in Lashgari et al. (2014). This finding motivated the present study where we focus on the particle dynamics to understand the two different underlying physical mechanisms.

Understanding the dynamics of particle dispersion and collisions, especially when the particle inertia is non-negligible and the suspension is not dilute, is therefore important due to their direct connection to the flow bulk properties, as also demonstrated in this study. The mutual and hydrodynamic interactions between the particles produce irregular motions, promote lateral migration from the instantaneous average particle trajectories and induce dispersion (for more details see Eckstein et al., 1977; Breedveld et al., 1998; Sierou and Brady, 2004). As an example, we report in Fig. 1 the instantaneous particle distribution for two different regimes: (i) a turbulent flow where transport is mainly determined by the Reynolds stresses and (ii) a shear-thickening flow dominated by the particle stress. Note that the wall normal direction is amplified by a factor 5 for the sake of clarity and the particle colors represent the magnitude of their translational velocities. We note a uniform concentration for the turbulent-like flow (left panel) and an accumulation towards the channel center for the flow dominated by the particle stress (right panel) that will be quantified and analyzed in this paper.

Particle collisions are also relevant to the total momentum transfer and can be estimated from the relative position and velocity of the particle pairs (Sundaram and Collins, 1997): these can be directly connected to the particle diffusivity in the cross-stream direction and to accumulation in specific regions (Cunha and Hinch, 1996; Reade and Collins, 2000; de Motta et al., 2012). The opposite is true for Brownian suspensions where the particle concentration variation arises from gradient-induced diffusivity (Breedveld et al., 1998), and finite-size effects are less important. In this work we show a strong shear-induced self-diffusivity at high particle volume fractions which is not dependent on the Reynolds number and plays an impor-
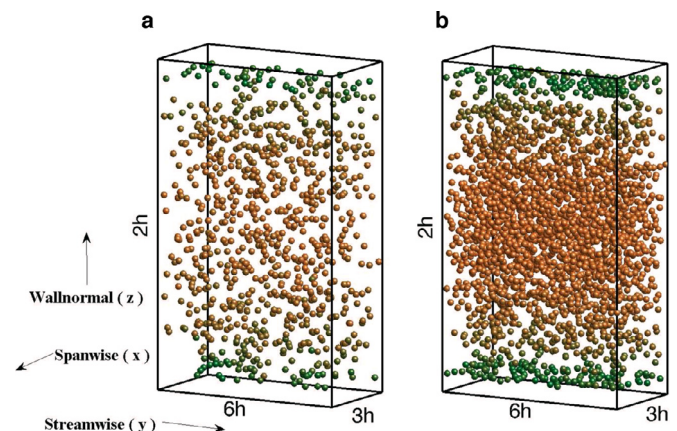

Fig. 1. The instantaneous particle arrangement for (a) a turbulent-like flow, $Re = 5000$ & $\Phi = 0.1$, and (b) a particle-stress dominated flow, $Re = 2500$ & $\Phi = 0.3$. The streamwise and spanwise coordinates and particle diameters are shown at their actual size, however the wall normal coordinate is stretched for a better visualization. The particle diameter is equal to $h/5$. (For interpretation of the references to color in this figure, the reader is referred to the web version of this article.)

tant role in the collision dynamics and eventually on the bulk flow behavior.

This paper is organized as follows. We discuss the governing equations, the numerical method and validations in Section 2. The results of the simulations are discussed in Section 3, whereas conclusions and final remarks are presented in Section 4.

Governing equations and numerical method

Governing equations

We study the motion of suspended rigid neutrally buoyant particles in a Newtonian carrier fluid. The Navier–Stokes and continuity equations govern the motion of the fluid phase,

$$\rho \left(\frac{\partial \mathbf{u}}{\partial t} + \mathbf{u} \cdot \nabla \mathbf{u} \right) = -\nabla P + \mu \nabla^2 \mathbf{u} + \rho \mathbf{f},$$

$$\nabla \cdot \mathbf{u} = 0, \tag{1}$$

where μ and P are the fluid viscosity and pressure respectively and ρ is the density of both fluid and particles. Here we denote the spanwise, streamwise and wall-normal coordinates as (x, y, z) with corresponding velocities $\mathbf{u} = (u, v, w)$, see Fig. 1. The force on the fluid, $\mathbf{f}$, is due to the presence of the finite-size particles. The motion of the particles is governed by the Newton–Euler equations

$$m^p \frac{d\mathbf{U}_c^p}{dt} = \mathbf{F}^p,$$

$$I^p \frac{d\mathbf{\Omega}_c^p}{dt} = \mathbf{T}^p, \tag{2}$$

where m^p and I^p are the mass and moment inertia of particle p, $\mathbf{U}_c^p$ and $\mathbf{\Omega}_c^p$ the velocity and rotation rate and $\mathbf{F}^p$ and $\mathbf{T}^p$ the net force and moment resulting from hydrodynamic and particle–particle interactions that for particles read

$$F^p = \oint_{\partial V_p} [-PI + \mu(\nabla \mathbf{u} + \nabla \mathbf{u}^T)] \cdot \mathbf{n} dS + \mathbf{F}_c,$$

$$T^p = \oint_{\partial V_p} \mathbf{r} \times \left\{ [-PI + \mu(\nabla \mathbf{u} + \nabla \mathbf{u}^T)] \cdot \mathbf{n} \right\} dS + \mathbf{T}_c. \tag{3}$$

In these equations ∂V_p represents the surface of the particles with unit normal vector $\mathbf{n}$. The radial distance from the center of the particle is denoted by $\mathbf{r}$ and the force and torque resulting from particle-particle (particle-wall) contacts are indicated by $\mathbf{F}_c$ and $\mathbf{T}_c$. The equations for the fluid and particle phase are coupled by the no slip and no penetration conditions on each point $\mathbf{X}$ on the surface of a particle, i.e. $\mathbf{u}(\mathbf{X}) = \mathbf{U}^p(\mathbf{X}) = \mathbf{U}_c^p + \mathbf{\Omega}_c^p \times \mathbf{r}$. We use here an Immersed Boundary Method (Breugem, 2012), where this condition is satisfied indirectly by applying the forcing $\mathbf{f}$ on the right hand side of the Navier–Stokes equations.

Numerical method

We employ a Navier–Stokes solver coupled with an Immersed Boundary Method (IBM) to follow the motion of the fluid and rigid spheres in the domain. The direct forcing method was originally proposed by Uhlmann (2005) and modified by Breugem (2012) to ensure second-order spatial accuracy. An Eulerian fixed mesh is used for the fluid phase and a Lagrangian mesh to represent the moving surface of the particles. The IBM forcing imposes no-slip and no-penetration boundary conditions on the surface of the particles. When the distance between particles or with a wall becomes smaller or of the order of the mesh size, the interactions between the particles include an additional lubrication correction. Surface roughness effects are accounted for at very close approach. Finally, a soft-sphere collision

model is employed to model collisions/contacts from the relative velocity and (slight) overlap of colliding particles. (see the Appendix of Lambert et al. (2013) for more details). The IBM code has been used to study passive and active suspensions by Lambert et al. (2013) and Picano et al. (2013, 2015).

Validation

The accuracy of the code has been verified against several test cases in Breugem (2012). In particular, the benchmark cases include:

(1) Flow through a regular array of spheres at solid volume fraction of 6.5% for which 2nd order accuracy has been shown together with excellent agreement with theoretical predictions in Hasimoto (1959).
(2) Lubrication force between 2 spheres: accurate predictions up to a gap width of 2.5% of the sphere radius at resolution $D/dx = 32$ (see Breugem (2010) and accuracy test at 1 specific gap width in Breugem (2012)).
(3) Drafting–kissing–tumbling interaction between two spheres for which 2nd order accuracy is confirmed.
(4) Validations of the global suspension behavior are reported in Picano et al. (2013, 2015).
(5) The code has also been compared with the experimental data by ten Cate et al. (2002) on a falling spherical particle in a closed rectangular container. The container dimensions were as in the experiment: $100 \times 100 \times 160$ mm^3 in the 2 horizontal and the vertical directions, respectively. The diameter of the nylon sphere was 15 mm. The mass density of the nylon sphere was 1120 kg/m^3. The mass density of the working fluid, silicon oil in this case, was 960 kg/m^3 (so the mass density ratio = 1.17). The dynamic viscosity of the working fluid is 0.058 kg/(ms) for estimated Reynolds number $Re \approx 31.9$. Fig. 2 shows the particle velocity as a function of time; the dots are the experimental data. The small difference at early time is probably related to the different release procedure in simulations and experiments.

In this work, we further validate the code by comparing the trajectory of a particle pair in homogeneous shear flow against the work of Kulkarni and Morris (2008a). These authors employ a Lattice-Boltzmann method to study the effect of particle inertia in a laminar flow. We choose the same box size of $20a \times 20a \times 20a$ with a the particle radius and place the origin of the coordinate system at the center of the box. The two particles are initially positioned at $\mathbf{X}_1 = (0, -4.85a, 0.32a)$ and $\mathbf{X}_2 = (0, +4.85a, -0.32a)$ and move
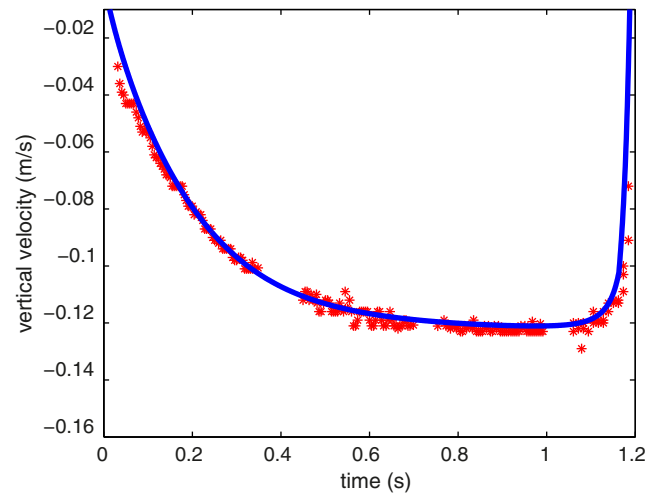

Fig. 2. Particle settling velocity versus observation time; the solid line represents the numerical results whereas the dots are the experimental data from ten Cate et al. (2002).
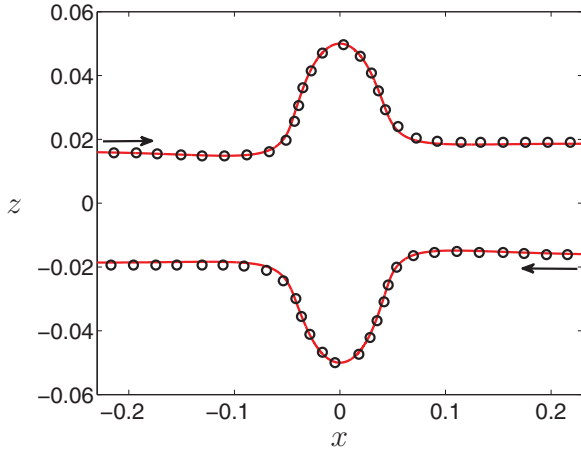
Fig. 3. Trajectory of a particle pair released in a simple shear flow from initial positions $\mathbf{X}_1 = (0, -4.85a, 0.32a)$ and $\mathbf{X}_2 = (0, +4.85a, -0.32a)$. The particle radius $a = 0.05$. The solid line indicates our simulation while open circles are the reference data in Kulkarni and Morris (2008a). The arrows show the initial direction of the particle velocities.

in opposite direction. The particle Reynolds number $Re_p = \frac{\dot{\gamma}a^2}{\nu} = 0.1$ with $\dot{\gamma}$ the imposed shear rate and ν the fluid kinematic viscosity. The initial particle velocity is the same as the local fluid velocity at the center of the particle and the initial rotation is equal to half the local fluid vorticity. The trajectory of the particle centers is displayed in Fig. 3 together with the data from Kulkarni and Morris (2008a) (open circles). The arrows display the direction of the particle velocity at the initial time. The results show a good agreement: the particle trajectories deviate away from the centerline after their interaction (a typical inertial effect).

Flow configuration and numerical setup

We simulate a channel flow with periodic boundary conditions in both streamwise and spanwise directions. The box-size is $6h \times 2h \times 3h$ in the streamwise, wall-normal and spanwise directions. The particles are neutrally buoyant and all have the same radius, $a = h/10$. The Reynolds number is defined as $Re = \frac{2hU_b}{\nu}$, where U_b is the fluid bulk velocity of the entire mixture and ν is the fluid kinematic viscosity. A wide range of parameters have been considered; the Reynolds number $500 \leq Re \leq 5000$, and the particle volume fraction $0 \leq \Phi \leq 0.3$. The number of particles for the highest volume fraction, $\Phi = 0.3$, is 2580. The simulations start with a high amplitude localized disturbance in the form of two counter-rotating streamwise vorticities (Henningson and Kim, 1991) to efficiently trigger turbulence, if the Reynolds number is high enough for it to be sustained (Lashgari et al., 2015). The particles are randomly positioned at time zero, with velocity equal to the local fluid velocity and rotation equal to half the local fluid vorticity.

For the simulations presented in this work we employ $480 \times 160 \times 240$ uniform Eulerian grid points in the streamwise, wall-normal and spanwise directions and 746 Lagrangian grid points to cover the surface of each particle. The simulation time to get the statistical convergence varies depending on the Reynolds number and particle concentration. As an example, for the case of $Re = 2500$ and $\Phi = 0.3$ we run for about 1100 time units corresponding to about 25,000 time steps. To check if the results are statistically converged, we repeat the analysis using half of the number of the samples and compare the outcome with the one from the total number of samples.

Results

In this work we study the local properties of the particulate flow, in particular particle distributions, dispersions and collisions, and connect the results with the bulk flow regimes identified in Lashgari et al. (2014).

Inertial regimes and Bagnold theory

In this section, we analyze in detail the momentum budget of the two phase flow and provide a comparison with the seminal work by Bagnold (1954). Batchelor (1970) was probably the first to derive an analytical expression for the bulk stress of suspensions of rigid particles and to discuss the relation between the macroscopic properties of a homogenous suspension and the flow structures at the particle scales. He assumed that (i) the bulk stress depends on the instantaneous particles configuration in a flow element containing a large number of particles; and (ii) the configuration in each element depends on the history of the motion (memory effect). This shows the importance of the local microstructure and of its time history to determine the bulk behavior of the suspension. For colloidal suspensions in the inertialess regime, the relation between the particle and bulk scale structures are thoroughly reviewed by Morris (2009).

We employ the phase-averaged momentum equations following the formulation developed in Marchioro et al. (1999), Prosperetti (2004) and Zhang and Prosperetti (2010) where the effect of spatial non-uniformity over a finite scale larger than the particle size has been taken into account, unlike in the original formulation by Batchelor. The phase average momentum equation on the volume $\mathcal{V}$ with boundary $\mathcal{S}(\mathcal{V})$ reads (Zhang and Prosperetti, 2010)

$$\rho \int_{\mathcal{V}} (\xi \boldsymbol{a}^p + (1-\xi)\boldsymbol{a}^f)\, d\mathcal{V} = \oint_{\mathcal{S}(\mathcal{V})} [\xi \boldsymbol{\sigma}^p + (1-\xi)\boldsymbol{\sigma}^f] \cdot n\, dS, \quad (4)$$

where ξ is the phase indicator with values $\xi = 0$ and $\xi = 1$ for the fluid and particle phases. The stress and acceleration of the fluid and particle phase are denoted by $\boldsymbol{\sigma}^f$, $\boldsymbol{a}^f$, $\boldsymbol{\sigma}^p$ and $\boldsymbol{a}^p$, respectively. Assuming statistical homogeneity in the streamwise and spanwise directions, one can obtain an expression for the stress budget across the channel (see for the detail of the derivations, the Appendix of Picano et al. (2015))

$$\frac{\tau(z/h)}{\rho} = -\langle v'^t w'^t \rangle + \nu(1-\varphi)\frac{dV^f}{dz} + \frac{\varphi}{\rho}\langle \sigma_{yz}^p \rangle = \nu \frac{dV^f}{dz}\bigg|_w \left(1 - \frac{z}{h}\right), \quad (5)$$

where $\tau(z/h)$ is the total stress as a function of wall normal coordinate, z, normalized by the channel half width, h, and V^f is the streamwise fluid velocity. The first term in the stress budget is the total Reynolds stress, $\frac{\tau_R}{\rho} = \langle v'^t w'^t \rangle = (1-\varphi)\langle v'^f w'^f \rangle + \varphi\langle v'^p w'^p \rangle$, consisting of the fluid and particle Reynolds stress weighted by local particle volume fraction, φ. The second term, $\frac{\tau_V}{\rho} = \nu(1-\varphi)\frac{dV^f}{dz}$, is the viscous stress whereas the third term, $\frac{\tau_P}{\rho} = \frac{\varphi}{\rho}\langle \sigma_{yz}^p \rangle$, is the stress due to the particles. The sum of the three terms is a linear function across the channel, as for a classic turbulent flow (Pope, 2000), with the wall shear stress $\frac{\tau_w}{\rho} = \nu \frac{dV^f}{dz}\big|_w$. The expression for the particle stress is discussed in detail in Batchelor (1970), Kulkarni and Morris (2008b) and Zhang and Prosperetti (2010). Following Batchelor (1970), the particle stress in the absence of an external torque reads

$$\sigma_{ij}^p = \frac{1}{V} \Sigma_V \int_{A_p} \frac{1}{2}\{\sigma_{ik}x_j + \sigma_{jk}x_i\}n_k dA$$
$$- \frac{1}{V}\Sigma_V \int_{V_p} \frac{1}{2}\rho\{f_i'x_j + f_j'x_i\}dV + \sigma_{ij}^c, \quad (6)$$

where x is the material point, f_i' is the local acceleration of the particle relative to the average acceleration, A_p and V_p are the particle
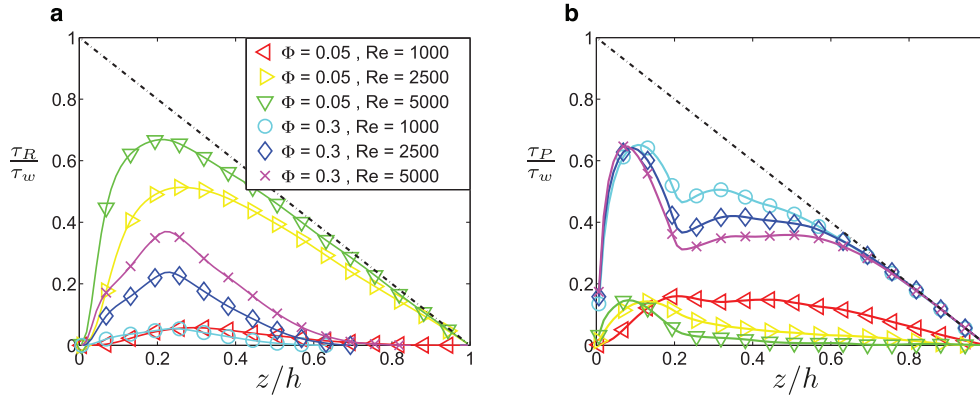
Fig. 4. Profiles of (a) the normalized Reynolds stress and (b) the particle stress across the channel for the cases indicated in the inset.

surface area and volume and $\sigma_{ij} = -P\delta_{ij} + \mu(\frac{\partial \mathbf{u}_i}{\partial x_j} + \frac{\partial \mathbf{u}_j}{\partial x_i})$ is the fluid stress tensor. The first term on the right hand side is the hydrodynamic stresslet resulting from the symmetric part of the shear stress. This is related to effective viscosity in dilute suspension (Prosperetti, 2004). The second term is the stress related to the particle acceleration and rotation with respect to the neighboring flow and the last term is the inter-particle stress which depends on the near-field particle interactions and particle collisions.

The wall-normal profiles of the normalized Reynolds and particle stresses, $\frac{\tau_R}{\tau_w}$ and $\frac{\tau_P}{\tau_w}$, are displayed in Fig. 4 for flows at low and high particle volume fractions, $\Phi = 0.05$ and $\Phi = 0.3$. The cases at $\Phi = 0.05$ and $Re > 2500$ are characterized by a dominant contribution of the Reynolds stresses with significant particle stress only in the near-wall region. At high volume fractions, $\Phi = 0.3$, on the contrary, the particle stress accounts for more than 75% of the total stress and the Reynolds stress is significant only in the intermediate region between the wall and centerline. As we will discuss in detail, the particle accumulation in the core region and in the layer close to the wall explains the high particle stress in the dense suspensions. Finally, we note that the major contribution to the total stress is due to the viscous forces at $\Phi = 0.05$ and $Re = 1000$. By increasing the Reynolds number at fixed Φ, the Reynolds stresses increase sharply when the flow becomes turbulent while the particle stress slightly decreases.

To understand the role of the different transport mechanisms on the bulk flow behavior in the range of Reynolds numbers and particle volume fractions investigated, we show in Fig. 5 (panels (a), (b), and (c)) maps of the relative contribution of viscous, Reynolds and particle stress to the total momentum transfer integrated across the channel. The dashed lines represent iso-levels of 25%, 50% and 75% of the total stress. The region where the viscous stress is more than 50% of the total stress is limited to $Re < 1900$ and $\Phi < 0.13$. In this region, the action of viscous dissipation overcomes inertia. The contour lines in Fig. 5(b) show the non-monotonic behavior of the Reynolds stress which is also an indication of the level of fluctuations in the flow. This trend is in agreement with previous experimental and numerical findings (Matas et al., 2003; Yu et al., 2013), where the authors report a non-monotonic behavior of the critical conditions for the occurrence of turbulent flow when increasing the particle volume fraction. The contribution of the Reynolds stress is more than 50% of the total for $Re > 2000$ and $\Phi < 0.1$: the fluid and particle phases induce strong fluctuations that cannot be damped by viscous dissipation. The region with $\Phi > 0.13$ is characterized by values of the particle stress larger than 50% of the total stress. In this region, we expect a high level of hydrodynamic and particle–particle interactions that induce strong particle stresses. Based on Fig. 5(b) and (c), the rate at which the particle stress contribution is increasing with Re is similar to the rate at which the Reynolds shear stress contribution is

increasing (the lines have similar slopes). This suggests that for high Φ the flow will not be dominated by turbulent transport when increasing the Reynolds number (Lashgari et al., 2014)

Finally, we display the effective viscosity in Fig. 5(d). Following previous literature, we define the effective viscosity as the normalized wall shear stress divided by the shear at the wall of the corresponding laminar flow, $\mu_r = \tau_w/\tau_0$ (Cokelet, 1999). We observe a monotonic increase of the dissipation when increasing both the Reynolds number and the particle volume fraction. The regions where the contribution of each stress term is more than 50% of the total (see panels (a), (b) and (c)) are depicted on the map of panel (d) by solid blue lines. Following Lashgari et al. (2014), these regions, shown in the direction of the arrows in panel (d), represent the laminar, turbulent and inertial shear-thickening regimes where the viscous, Reynolds and particle stress contribute the most to the momentum transfer. The three transport mechanisms coexist with different relevance depending on the Reynolds number and particle volume fraction.

To continue our analysis, we first recall the work by Bagnold (1954) on inertial suspensions. This author introduces what is known as the Bagnold number, $Ba = 4Re_p\sqrt{\lambda}$, where $\lambda = \frac{1}{(0.74/\Phi)^{1/3}-1}$ is the linear concentration computed as the ratio between the particle diameter and the average radial separation distance and Re_p, the particle Reynolds number. This non-dimensional parameter represents the ratio between inertial and viscous stresses and it is shown to describe the bulk behavior of the suspensions reasonably well. Bagnold defines a macro-viscous regime, $Ba < 40$, at low Reynolds number and low particle volume fraction where the relation between the stress and shear-rate is linear (similar to a Newtonian flow). The Bagnoldian regime, instead, $Ba > 450$, appears at higher Reynolds numbers and particle volume fractions and is characterized by a quadratic dependence of the stress on the shear-rate.

The effective viscosity pertaining our simulations is depicted versus the Bagnold number in Fig. 6 for four representative values of the particle volume fraction. Interestingly, we observe that the effective viscosity of the suspension is almost constant when $Ba < 40$, as expected in the macro-viscous regime where the shear stress depends linearly on the Bagnold number (constant effective viscosity). When $Ba > 70$, all the curves collapse on a single line (see Fig. 5(d)) and the effective viscosity varies linearly with the Bagnold number.

These results suggest that both the Reynolds and particle stress dominated flows fall into the Bagnoldian inertial regime: the same value of the Bagnold number and the same dissipation (effective viscosity) may therefore be explained by two different underlying physical mechanisms. The shear stress due to the residual turbulence becomes negligible when increasing the grain concentration, as predicted by Bagnold, and the particle stress takes the place of the Reynolds stress in the transport of momentum across the channel. At
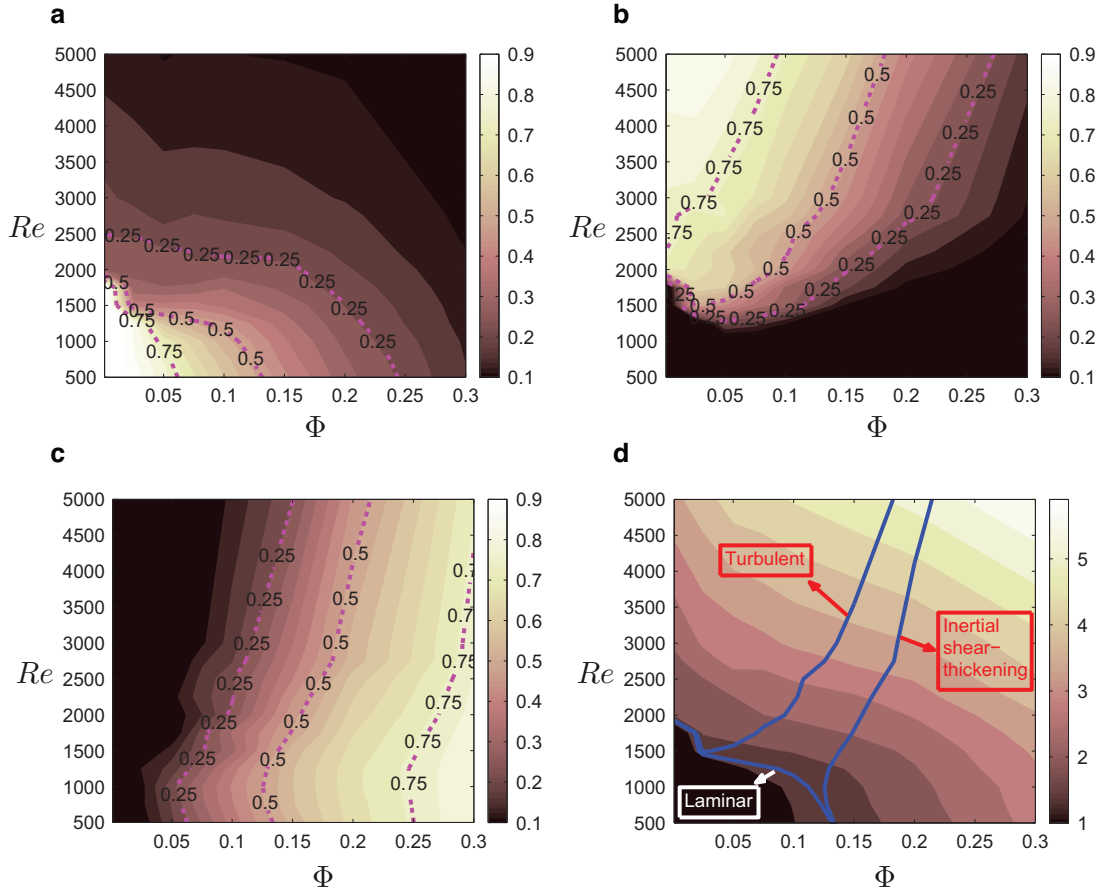
Fig. 5. Contour map of the percentage contribution of (a) viscous stress, (b) Reynolds stress and (c) particle stress to the total momentum transport integrated across the channel. The isolines show the boundary of the regions in the map where the contribution of each term is more than 25%, 50% and 75%. (d) Contour map of effective viscosity, the normalized wall shear stress divided by the shear at the wall of the corresponding laminar flow. (For interpretation of the references to color in this figure, the reader is referred to the web version of this article.)
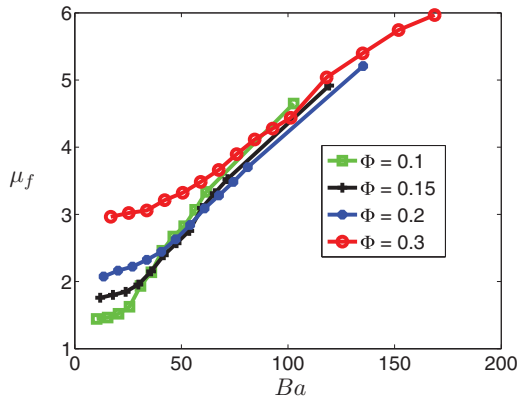

Fig. 6. Effective viscosity, the normalized wall shear stress divided by the shear at the wall of the corresponding laminar flow, $\mu_r = \tau_w/\tau_0$, versus Bagnold number for four representative values of the volume fraction ϕ.

very high volume fraction the dynamics of the flow resemble granular media where the effect of interstitial fluid is negligible and the interparticle collision is the main transport mechanism (Balachandar and Eaton, 2010).

Single particle statistics

The single particle statistics are computed by considering quantities related to each individual particle and taking ensemble aver-

age over time and space. In particular, we extract the local volume fraction, mean and rms velocities of the particles as a function of the wall-normal coordinate z.

The wall-normal profiles of the local particle volume fraction are shown in Fig. 7 for different Reynolds numbers and particle volume fractions, covering the three different regimes introduced above. Based on the phase diagram in Fig. 5(d), we see that in the laminar regime the particles accumulate in the intermediate region between the wall and the channel centerline, $0.2 \lesssim z/h \lesssim 0.8$ (cf. data for $Re = 500$, $\Phi = 0.05$ and $\Phi = 0.1$). This appears to be due to the Segre–Silberberg effect (Segré and Silberberg, 1961), an inertial effect (inertial migration) resulting from particle–fluid interactions, in particular explained in the dilute regime by the balance between the Saffman lift (Saffman, 1965) and inhomogeneous shear rate and wall effects (see also McLaughlin, 1991, 1993; Cherukat and McLaughlin, 1994; Schonberg and Hinch, 1989). The Segre–Silberberg effect is documented also at finite Reynolds numbers and volume fractions in the work by Matas et al. (2004) where it is shown that the particle equilibrium position moves closer to the wall when increasing the Reynolds number, i.e. increasing inertial effects.

The data in the figure show that increasing the Reynolds number while keeping a low volume fraction the flow becomes turbulent and the particle distribution is almost uniform across the channel, except in the near wall region due to the one sided wall–particle interactions. The particle distribution is homogenized by the action of the Reynolds stresses for the flow cases at $Re = \{2500, 5000\}$ and $\Phi = \{0.05, 0.1\}$, which are in the turbulent region of the phase diagram in Fig. 5(d).
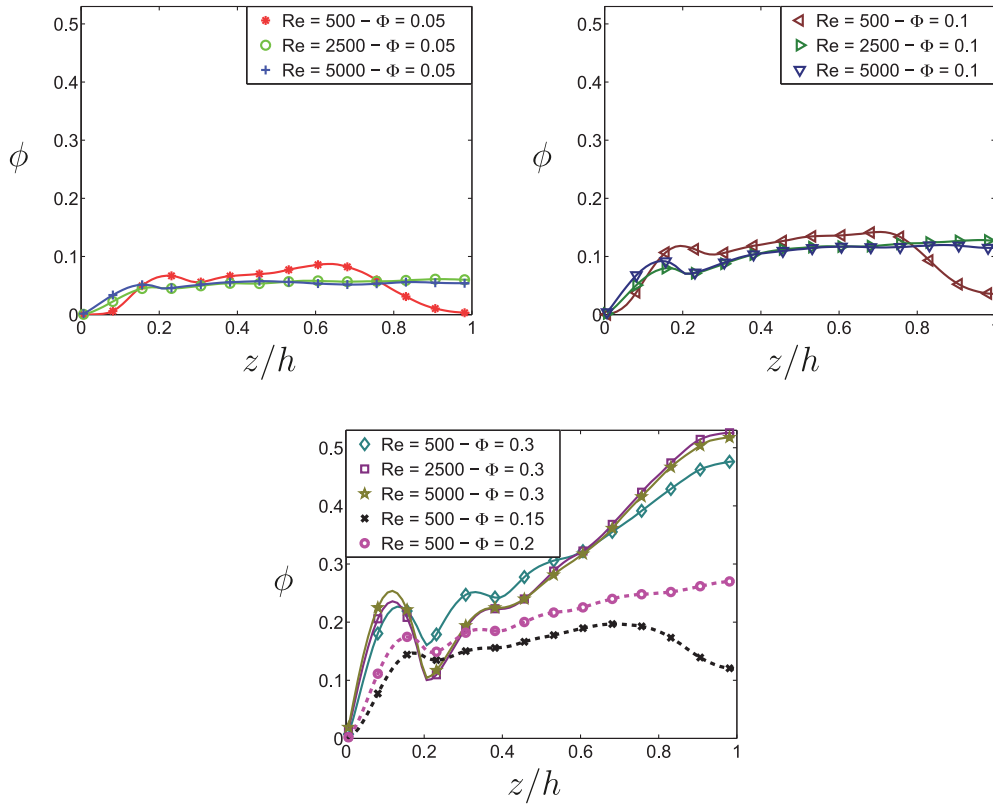
Fig. 7. Wall-normal profiles of the local volume fraction for different values of the Reynolds number *Re* and volume fraction Φ, see inset.

The particle distribution in the inertial shear-thickening regime, i.e. Φ = 0.3, exhibits a completely different behavior with a significant accumulation of the particles in the core region. The tendency of the particles to migrate toward the channel centerline is not *per se* an inertial effect (shear-induced migration) and is attributed to the imbalance of the normal stresses in the wall-normal direction (see Fall et al., 2010; Yeo and Maxey, 2011; Guazzelli and Morris, 2011, for more details). When particle layers are sheared over each other, normal particle stress tends to push the particle layers further apart from each other which causes migration towards the core. Nott and Brady (1994) first documented particle migration towards the core region at *Re* = 0. This effect is also evident from the data presented here as the profile of the local volume fraction does not change considerably increasing the Reynolds number from 500 to 5000. The local particle volume fraction in the core region approaches the value for a random loose packing; here the particles experience an almost uniform translational velocity, of the same magnitude as the carrier flow in some sort of plug flow, see discussion below. We find a peak of the local particle volume fraction at $z/h = 0.1$ also at the highest volume fraction under investigation, corresponding to particle layering at the wall. Once a particle approaches the wall it tends to stay there because the interaction with neighboring suspended particles is asymmetric and the strong near-wall lubrication force hinders departing motions.

We finally note that, as we increase the particle volume fraction above Φ = 0.2 at fixed Reynolds number, *Re* = 500, the particle distribution changes from that typical of the Segre–Silberberg effect (due to the fluid–particle interactions) to display a significant accumulation in the core region due to the particle–particle interactions (shear-induced migration).

The mean and rms particle velocities are depicted in Fig. 8 for some of the representative cases above. Fig. 8(a) shows the mean streamwise velocity component to highlight the slip velocities at the

wall. The velocity profile is closer to the parabolic single-phase profile for the laminar cases, while it becomes blunt in the turbulent and inertial shear-thickening regimes. Increasing the Reynolds number, the mean flow becomes more uniform across the channel. The fluctuation (rms) velocities, Fig. 8(b)–(d), have also nonzero values at the wall: the level of fluctuations is higher for the turbulent cases and lower for the laminar flows, as expected. Interestingly, the level of particle velocity fluctuations of the inertial shear thickening regime (in particular for the cases *Re* = 2500, Φ = 0.3 and *Re* = 5000, Φ = 0.3) is similar to that of the turbulent flows closer to the wall, $z/h < 0.35$, and closer to the laminar values towards the centerline, $z/h > 0.65$. This observation suggests that the dynamics of the inertial shear-thickening flows are similar to that of the laminar flow in the core of the channel and to that of the turbulent flow in the near-wall region. The low level of fluctuations in the core region results from the significant particle accumulation discussed above, which also explains the large particle stress in the inertial shear-thickening regime. Finally, we note that the peak of the wall-normal velocity fluctuations is located at $z/h = 0.1$ for all the cases (except *Re* = 500 and Φ = 0.05), indicating the relevance of the impact with the wall. The peak moves to $z/h = 0.2$ for the streamwise and spanwise components of the velocity fluctuations.

Particle dispersion

To understand the dynamics of the interactions in the flow, we study the particle dispersion. The hydrodynamic and particle–particle interactions induce lateral forces and diffuse the particles away from their initial path. The dispersion is quantified by the variance of the particle displacement (Cunha and Hinch, 1996; Janoschek, 2013). Here, we compute the mean-square displacement of the particle trajectories, $\mathbf{X}_p(t) = [x_p(t), y_p(t), z_p(t)]$, as a function of the time interval Δt, averaging over all times, t, and particles, p, sampling after the initial transient in the flow development. For the
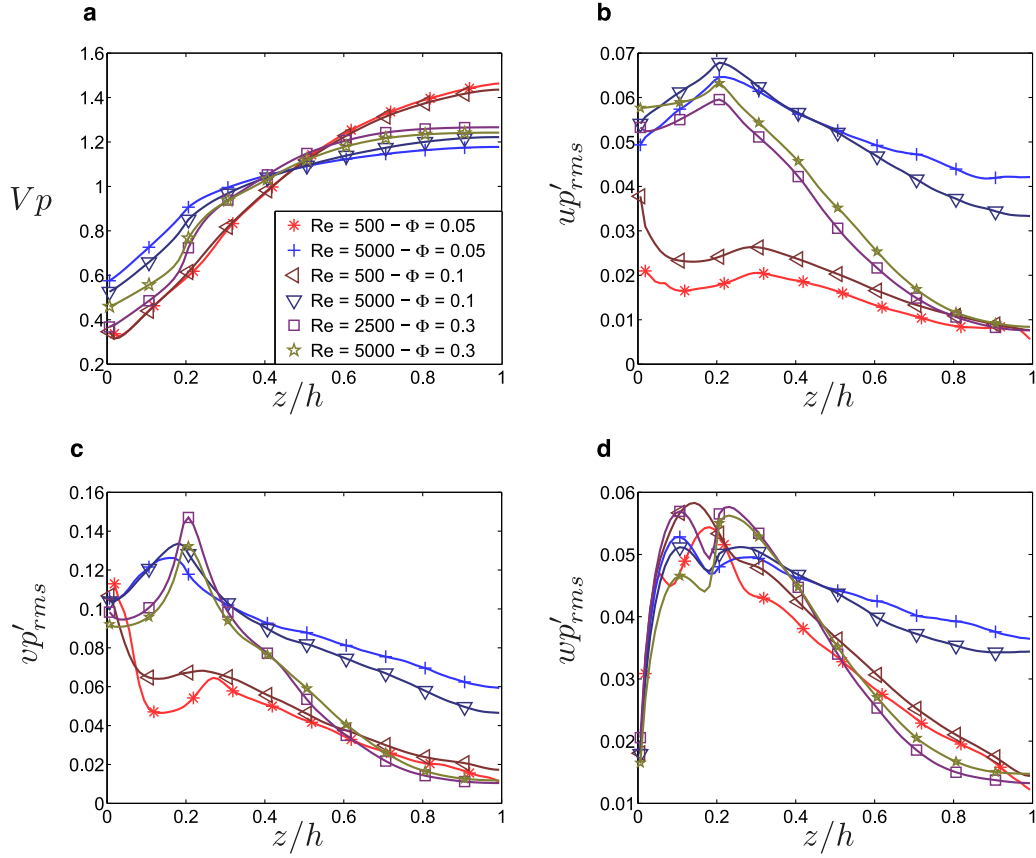
Fig. 8. Wall-normal profiles of the mean particle streamwise velocity component and of the 3 particle rms velocities for the different values of Re and Φ indicated by the inset.

spanwise component, $x_p(t)$, it reads

$$\langle \Delta x_p^2(\Delta t) \rangle = \langle [x_p(t + \Delta t) - x_p(t)]^2 \rangle_{p,t}. \tag{7}$$

The sampling time for diffusion must be larger in the case of lower Φ, since the fewer interactions between the particles require more time to reach the statistical convergence (Sierou and Brady, 2004). The particle diffusion coefficients in the spanwise direction can then be calculated by measuring the slope of the mean square displacement, at large Δt,

$$D_{xx} = \frac{\langle \Delta x_p^2(\Delta t) \rangle}{2\Delta t}. \tag{8}$$

The normalized correlation of the spanwise displacements is defined by

$$R_{xx}(\Delta t) = \frac{\langle x_p(t + \Delta t) x_p(t) \rangle_{p,t} - \langle x_p(t) \rangle^2}{\langle x_p(t)^2 \rangle - \langle x_p(t) \rangle^2}, \tag{9}$$

and it is used to quantify memory effects. The particle correlation and mean square displacement can be directly connected, only for large Δt, by

$$R_{xx}(\Delta t) = 1 + \frac{-D_{xx}\Delta t}{\langle x_p(t)^2 \rangle - \langle x_p(t) \rangle^2}. \tag{10}$$

The same algebra applies for the other components. The spanwise mean square particle displacement, defined by Eq. (7), is displayed in Fig.9(a) and (c) as a function of $\dot{\gamma}\Delta t$ where $\dot{\gamma} = \frac{U_b}{h}$ is the average shear-rate across the channel. For all the cases studied, the mean square dispersion grows initially quadratically. In this ballistic regime, the particle trajectories are correlated and the displacements are proportional to Δt so that $\langle \Delta x_p^2(\Delta t) \rangle \propto (\Delta t)^2$. The trend changes for larger time lags when the classical diffusive behavior is retrieved. This is induced by particle–particle and hydrodynamic interactions that de-correlate the trajectories in time as shown among

others by Sierou and Brady (2004) and Janoschek (2013) in Stokes and low Reynolds number flows. The asymptotic slope determines the dispersion coefficient: the highest mean square displacements are found for $Re = 2500 - 5000$ and $\Phi = 0.05 - 0.1$ in the turbulent regime. The strong fluctuations de-correlate the particles trajectories in shorter time and promote higher dispersion. The lowest dispersion is obtained in the simulations at $Re = 500$ and $\Phi = 0.05 - 0.1$, i.e. in the laminar regime where the viscous stress is dominating the flow dynamics, see Fig. 5.

The asymptotic trend of the mean square displacement of the cases at $\Phi = 0.3$ lies in between those of the turbulent and laminar regimes and smoothly increases with the Reynolds number. The two dashed black lines in the figure represent therefore the lower and upper limit attained at $Re = 500$ and $Re = 5000$, the other cases are lying in between. Thus, in the cases for which the particle stress provides the largest contribution to the momentum transfer (inertial shear-thickening), the diffusion coefficients are well below those of a turbulent flow. In the core region, the particle dispersion is low due to the significant particle accumulation, of the order of that in a laminar flow. However, the turbulent stress is still active (see Fig. 4(a)) in the intermediate region between the wall and the centerline, which locally increases mixing. This explains why the overall dispersion in the inertial shear thickening regimes is between that of the laminar and turbulent regimes, as shown in Fig. 9. The Reynolds stress and particle stress dominated regimes exhibit therefore different values of the particle dispersion even if they assume the same value of the Bagnold number.

The wall-normal mean square particle displacement is depicted in Fig. 9(b) and (d). First, we note that the wall-normal dispersion is lower than its spanwise counterpart due to the presence of the walls. The data in Fig. 9(b) and (d) asymptotically approach the value 18^2, the maximum possible wall-normal displacement when normalized
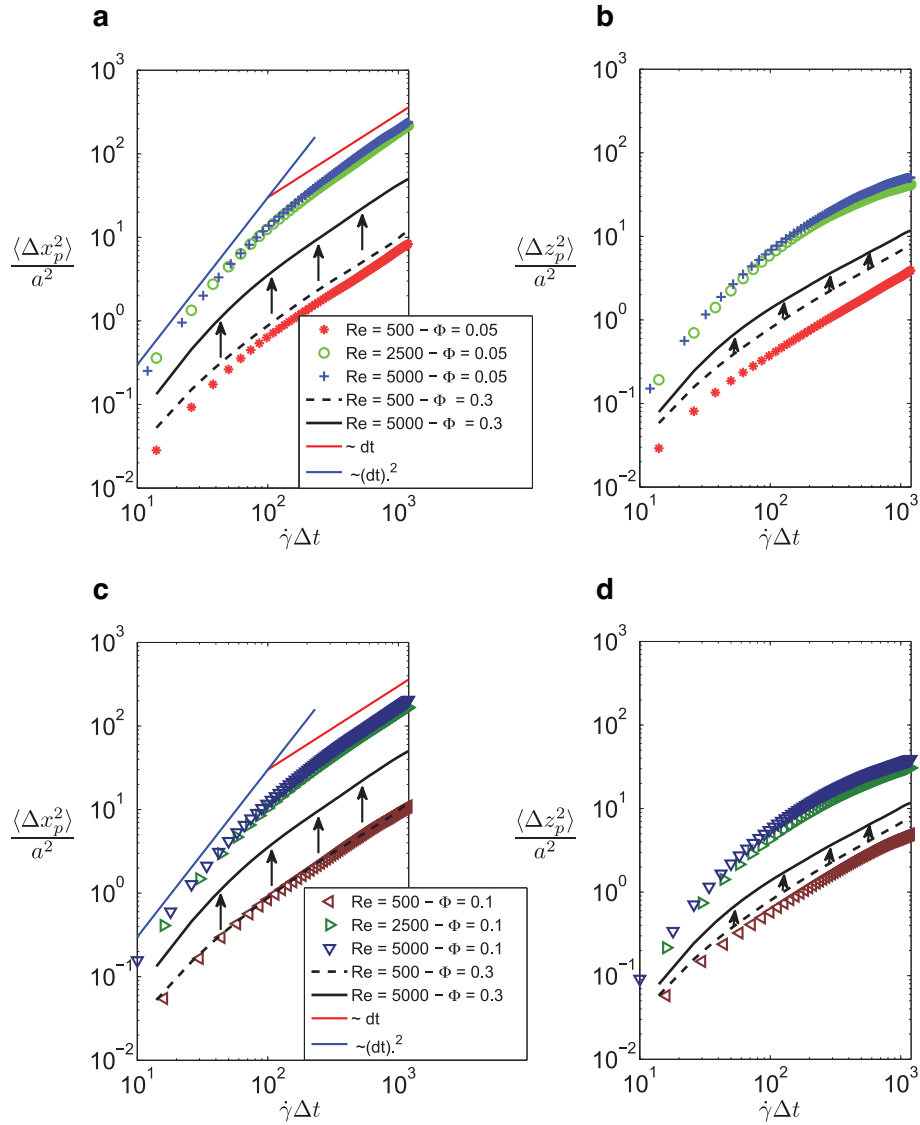
Fig. 9. Mean square particle displacement in the spanwise (a, c) and wall-normal direction (b, d) for the cases indicated in the inset. The thick black lines with arrows indicate the range of values assumed by flows in the inertial shear-thickening regime.

with the particle radius. As observed for the spanwise dispersion, the highest and lowest diffusion pertain to the turbulent and laminar flows, whereas inertial shear-thickening flows display intermediate values. These data on single-particle dispersion provide additional evidence that two distinct dynamics are at work in the turbulent or inertial shear-thickening regime, despite they can be both classified as inertial Bagnoldian flows.

The values of the spanwise dispersion coefficients extrapolated for larger Δt from the data in Fig. 9 are reported in Table 1. The largest dispersion coefficient is obtained for the case $Re = 5000$ and $\Phi = 0.05$ where the turbulence activity is the strongest and the lowest one for $Re = 500$ and $\Phi = 0.05$ in the laminar regime. As mentioned above, the wall-normal mean square displacement is limited by the walls and therefore its slope does not reach a constant value, corresponding to a well-defined value of the wall-normal dispersion coefficient.

Particle-pair statistics

We shall also consider the variations of quantities pertaining pairs of particles as a function of the distance between their centers, r. As r

approaches the particle diameter, the near field interactions become important and collisions occur when r become less than one particle diameter. For the details of pair-particle statistics the reader is referred to the Appendix of Sundaram and Collins (1997) among others. Here, we shortly introduce the Radial Distribution Function, $g(r)$. In a reference frame with origin at the center of one particle, the RDF is the averaged number of particle centers located in a shell of radius r and $r + dr$ divided by the expected number of particles of a uniform distribution (see Reade and Collins, 2000; Gualtieri et al., 2009). Formally, $g(r)$ is defined as

$$g(r) = \frac{1}{4\pi} \frac{dN_r}{dr} \frac{1}{r^2 n_0}, \qquad (11)$$

where N_r is the number of particle pairs in a sphere of radius r and $n_0 = 0.5 * N_p(N_p - 1)/V$ the density of particle pairs in the volume V, with N_p the total number of particles. For small values of r, $g(r)$ reveals the intensity of the particle clustering whereas $g(r) \to 1$ when $r \to \infty$ (uniform distribution).

The dynamics of the particle pair cannot be determined only by the pair distribution function. Following the study of Sundaram and Collins (1997), we compute the normal relative velocity of the particle

Table 1
Dispersion coefficients computed by particle displacements in the spanwise direction.

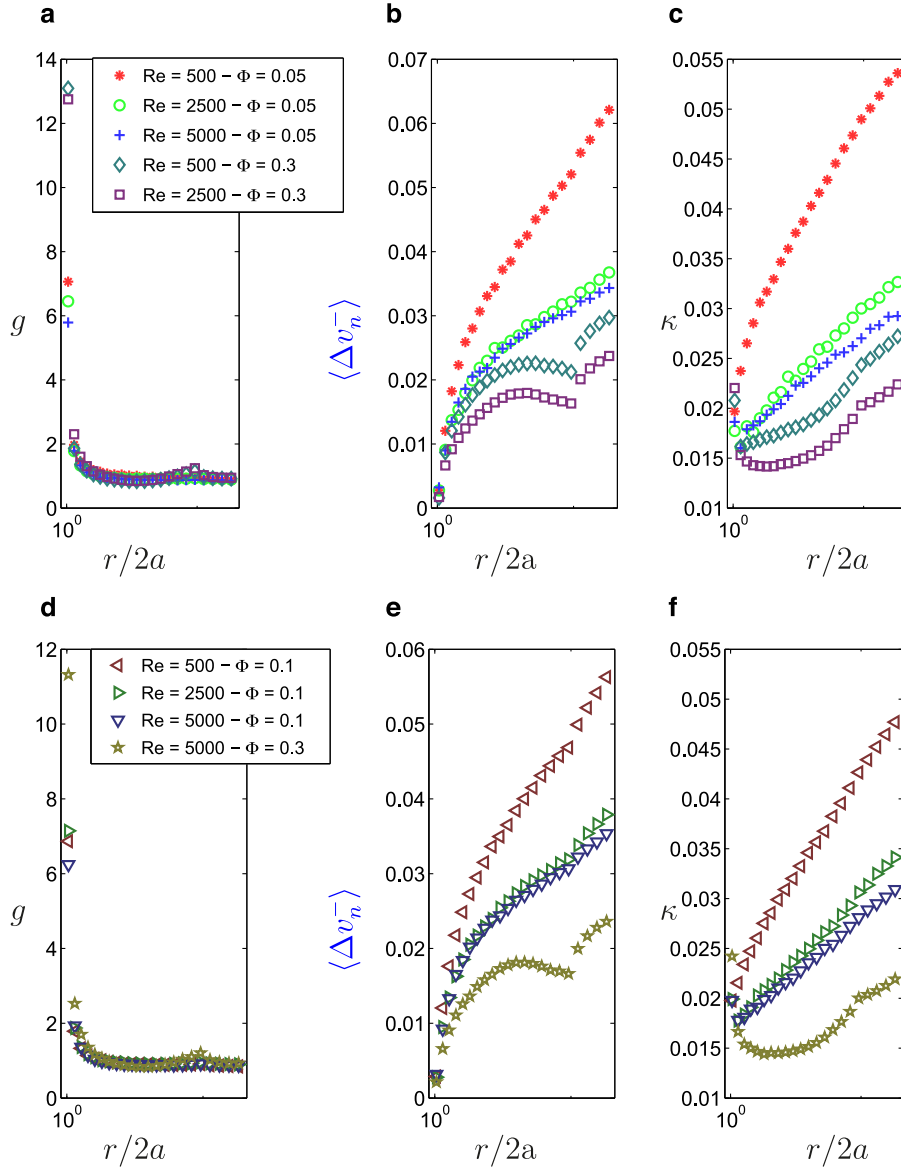| Re	500	2500	5000	500	2500	5000	500	2500	5000
Φ	0.05	0.05	0.05	0.1	0.1	0.1	0.3	0.3	0.3
$\frac{D_x}{\dot{\gamma}a^2}$	0.004	0.095	0.1	0.005	0.075	0.085	0.005	0.018	0.023

Fig. 10. (a, d) Pair distribution function, $g(r)$; (b, e) magnitude of relative normal velocity, $\langle \Delta v_n^-(r) \rangle$; (c, f) magnitude of collision kernel $\kappa(r) = g(r) \cdot \langle \Delta v_n^-(r) \rangle$ as a function of the distance between the particle-pair, r, for different values of Re and Φ.

pairs as function of r. Considering particles i and j, the normal relative velocity of the particle pair is obtained as the inner product of their relative velocity and relative distance (see Gualtieri et al., 2012)

$$\Delta v_n(r_{ij}) = (\mathbf{u}_i - \mathbf{u}_j) \cdot \frac{(\mathbf{r}_i - \mathbf{r}_j)}{|(\mathbf{r}_i - \mathbf{r}_j)|} = (\mathbf{u}_i - \mathbf{u}_j) \cdot \frac{\mathbf{r}_{ij}}{|\mathbf{r}_{ij}|}. \quad (12)$$

The normal relative velocity is a scalar quantity and can be either negative, $\Delta v_n^-(r_{ab}) = \Delta v_n(r_{ab})\big|_{<0}$, for approaching particles or positive, $\Delta v_n^+(r_{ab}) = \Delta v_n(r_{ab})\big|_{>0}$, when the two particles depart from each other. The averaged normal relative velocity can be therefore decomposed into $\langle \Delta v_n(r) \rangle = \langle \Delta v_n^+(r) \rangle + \langle \Delta v_n^-(r) \rangle$. Finally, the collision kernel is obtained as the product of $g(r)$ and $\langle \Delta v_n^-(r) \rangle$ (Sundaram

and Collins, 1997),

$$\kappa(r) = g(r) \cdot \langle \Delta v_n^-(r) \rangle. \quad (13)$$

First we compute the Radial Distribution Function, $g(r)$, the normalized probability of finding pair of particles at distance r. The results are shown in Fig. 10(a) and (d) for several cases covering the three different regimes. For all the cases, the maxima of $g(r)$ occur at $r/2a = 1$ where the particles are in contact and the collision force is active. Note that to compute the RDF, r is discretized in the range of $r/2a = [0.9, 4]$ and the data for $r/2a < 1$ are not displayed (we may have some events where $0.9 < r/2a < 1$). Increasing the distance between the particles, $g(r) \rightarrow 1$, as expected. The inertial shear-thickening cases are characterized by the highest value of $g(r/2a = 1)$ and by an additional peak around $r/2a = 2$ indicating the probability
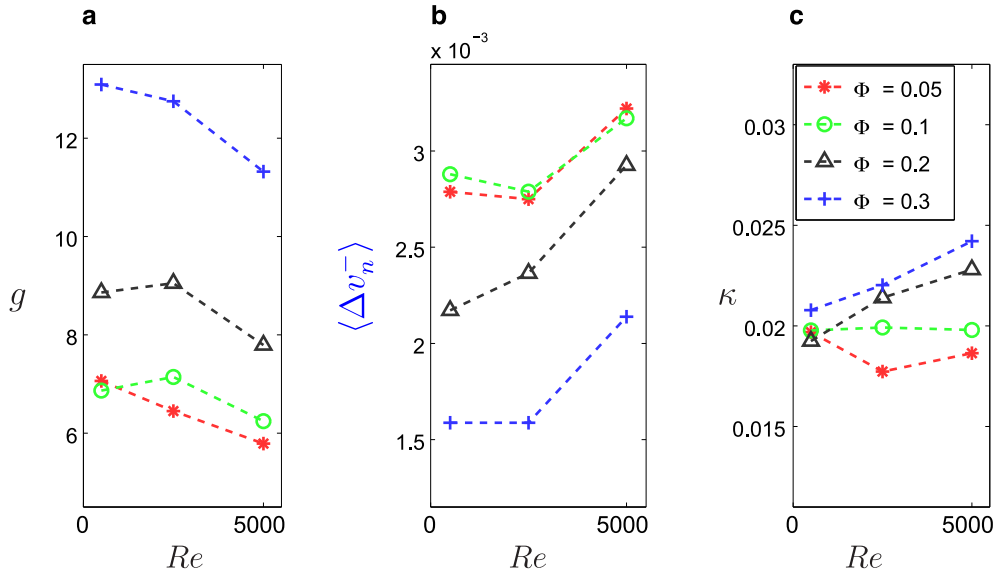
Fig. 11. (a) Pair distribution function, $g(r = 2a)$; (b) magnitude of relative normal velocity, $\langle \Delta v_n^- \rangle (r = 2a)$; (c) magnitude of collision kernel $\kappa \, (r = 2a) = g(r = 2a) \cdot \langle \Delta v_n^- (r = 2a) \rangle$ versus the Reynolds number for the indicated values of the volume fraction Φ.

of finding a second layer of the particles. In all the cases, the peak of $g(r)$ decreases slightly when increasing the Reynolds number as the inertia tends to decorrelate the particle paths.

We then study the normal relative velocity as function of r, $\langle \Delta v_n(r) \rangle$. We show the statistics of the magnitude of the negative relative velocity, $\langle \Delta v_n^-(r) \rangle$, in Fig. 10(b) and (e); this observable indicates the tendency of the particle pairs to approach each other. The relative velocity increases almost monotonically with r as the pairs are more likely to approach with higher speed when farther away. The highest values of $\langle \Delta v_n^-(r) \rangle$ occur for the laminar cases and the lowest in the inertial shear-thickening regime, also the densest cases (again the relative negative velocity increases smoothly with the Reynolds number for $\Phi = 0.3$). The turbulent and inertial shear thickening flows (the Bagnoldian inertial flows) both exhibit values of $\langle \Delta v_n^-(r) \rangle$ lower than the laminar flows.

The physical mechanism for the reduction of $\langle \Delta v_n^-(r) \rangle$ is however different. While the turbulent flow tend to homogenize the suspension, the shear induced migration observed in the inertial shear-thickening regime produces a significant accumulation in the core region where the particles are transported downstream by the core flow at almost constant velocity. This suggests that inertia and turbulent eddies determine the local and bulk behavior of the suspensions at low particle volume fraction, whereas particle interactions and shear-induced migration governs the behavior of the flow at high particle volume fractions. The latter effect being almost independent of the flow inertia as discussed above.

Using single particle statistics, we have shown that the particle dispersion is highest, moderate and low for the turbulent, inertial shear-thickening and laminar flows respectively. On the other hand, the analyses of the particle-pair statistics, i.e. relative velocity, show the opposite ordering (laminar, turbulent and inertial shear-thickening regimes from high to low). This indicates that these two different aspects of the particle dynamics reflect the presence of the three different bulk regimes in a different fashion.

The collision kernel, the product of $g(r)$ and $\langle \Delta v_n^-(r) \rangle$, is depicted in Fig. 10(c) and (f). Similarly to the normal relative velocities, this kernel increases monotonically with the distance r. Interestingly, the kernel assumes similar values when the particles are in contact $(r/2a = 1)$ for all the cases studied.

To explain the observation that the kernel function has similar values at contact, we display in Fig. 11 the separate contribution of $g(r)$ and $\langle \Delta v_n^-(r) \rangle$ to the kernel at $r/2a = 1$. We set the range of the vertical axes to cover $\pm 50\%$ of the mean values of the data in each plot to ease a visual comparison. The values of $g(r/2a = 1)$ and $\langle \Delta v_n^-(r/2a = 1) \rangle$ are almost independent of the Reynolds number; they do however increase and decrease with the particle volume fraction in such a way that their product is almost constant and equal to $0.022 \pm 10\%$ for the collision kernel at $r/2a = 1$. This unique value seems to be valid for all the Reynolds numbers and particle volume fractions studied in the present work as well as those in Lashgari et al. (2014). Note that the statistical error bar for the kernel at $r/2a = 1$ is about 1%.

As shown above, the dynamics of the particles changes considerably across the channel. To this end, we divide the channel into two regions: region I, close to the walls ($0.05 < z/2h < 0.35$ and $0.65 < z/2h < 0.95$) and region II the middle of the channel ($0.35 < z/2h < 0.65$). Note that the particle centers move in the range $0.05 < z/2h < 0.95$, as the particle radius $a = 0.05$.

We thus examine the radial distribution function, negative normal relative velocity and the kernel operator in these regions, limiting the analysis to three flow cases representing the laminar, turbulent and inertial-shear thickening regimes, see Fig. 12. Note that $g(r)$ is normalized by the total number of particle pairs in each of the two regions. The normal relative velocity, see Fig. 12(b), is higher in the near-wall region for all the three cases, a fact attributed to the strong background shear, however the difference decreases when the turbulent activity increases. The collision kernels, see Fig. 12(c), reveal that the kernel of the inertial shear-thickening flow, $Re = 2500$ and $\Phi = 0.3$, is similar to that of the turbulent flow, $Re = 5000$ and $\Phi = 0.1$, near the walls and to that of the laminar flow, $Re = 500$ and $\Phi = 0.05$, in the flow bulk. This is inline with the results in Fig. 8 pertaining the particle velocity fluctuations.

For the inertial shear-thickening flow, the radial distribution function at contact, $g(r/2a = 1)$, is higher in region II. The difference between regions I and II is reduced for the turbulent flow, reflecting the more uniform particle distribution. The opposite behavior is observed in the laminar regime where $g(r/2a = 1)$ is instead slightly higher in region I.
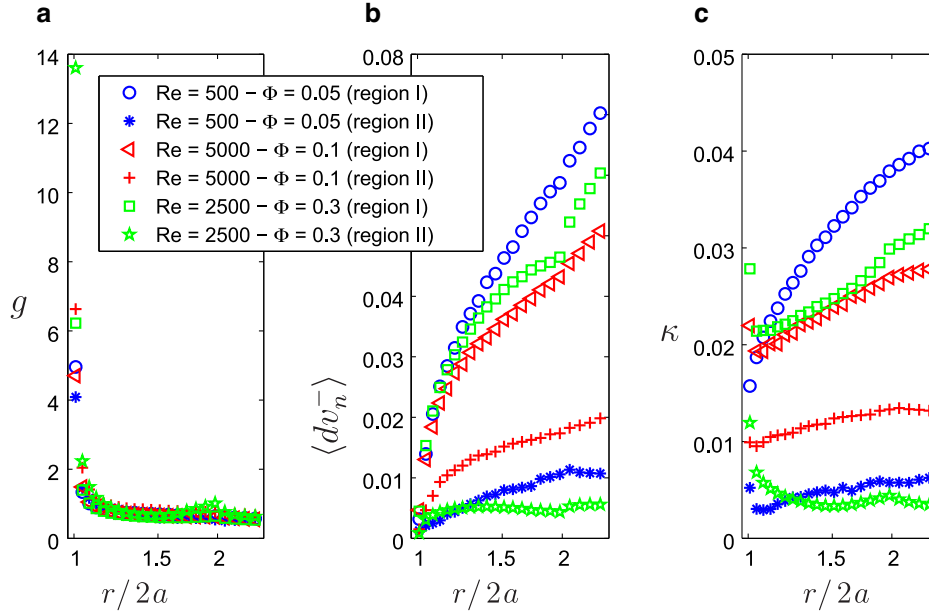
Fig. 12. (a) Pair distribution function, (b) magnitude of relative normal velocity, (a) magnitude of collision kernel as a function of distance between the particle-pair, r, in the near-wall region I and channel core region II for three configurations. Laminar flow: $Re = 500$ & $\Phi = 0.05$, inertial shear-thickening flow: $Re = 2500$ and $\Phi = 0.3$ and turbulent flow: $Re = 5000$ and $\Phi = 0.1$.

Conclusion and remarks

We study the flow of suspensions of the finite-size neutrally buoyant particles in a channel, aiming to connect the local particle behavior to the bulk flow properties. The analysis is based on data from direct numerical simulations covering a wide range of Reynolds number, $500 \leq Re \leq 5000$, and particle volume fraction, $0 \leq \Phi \leq 0.3$, where the particles are rigid spheres with fixed ratio between the particle diameter and channel height of 1/10.

The analyses of the stress budget reveal the existence of the three different flow regimes: laminar, turbulent and inertial shear-thickening depending on which of the stress terms, viscous, Reynolds or particle stress, is the major responsible for the momentum transfer across the channel. We show that both Reynolds and particle stress dominated flows fall into the Bagnoldian inertial regime (Bagnold, 1954): the suspension effective viscosity, i.e. the normalized wall shear stress, from the different simulations collapses when plotted versus the Bagnold number. Therefore, turbulent and inertial shear-thickening flows may share the same Bagnold number while the underlying momentum transport and dissipation are distinct.

Examining the particle distribution we show that in the viscosity dominated laminar flows, characterized by low particle volume fraction and Reynolds number ($\Phi < 0.1$ and $Re < 1000$), the particles tend to accumulate at certain wall-normal equilibrium positions, a clear signature of the Segre–Silberberg effect. The turbulent particle-laden flow, $\Phi < 0.1$ and $Re > 1500$, is instead characterized by a more uniform particle distribution due to the mixing by the turbulent eddies. At high volume fractions, $\Phi > 0.2$, we report a significant migration of the particles toward the channel centerline for all the Reynolds numbers under investigation, which explains the large contribution of the particle stress in the so-called inertial shear-thickening regime. The particle accumulation in the core region is not necessarily an inertial affect as we observe a negligible variation of the local particle volume fractions when increasing the Reynolds number.

The mean particle velocity profile becomes more blunt as the flow regime changes from laminar to either turbulent or particle-dominated shear-thickening. Interestingly, the velocity fluctuation amplitudes pertaining the inertial shear-thickening are closer to those of the turbulent flow in the near wall region, while they almost

overlap to those of the laminar flow in the vicinity of the channel centerline. The particle dynamics in the inertial shear-thickening regime appear therefore to share similarities with both the laminar and turbulent flow depending on the wall-normal position. This is further confirmed by examining the spanwise and wall-normal particle dispersion. For the inertial shear-thickening flows the turbulent activity is limited to the near-wall region while in the center of the channel the particles form a dense layer and are transported by the smooth flow of the carrier fluid. As a result of this, the dispersion coefficients of the inertial shear-thickening regime lie in between those of the two other regimes. Finally, we note that both the mean and fluctuating particle velocities exhibit slip velocities at the wall.

We further consider the pair particle statistics in the three different regimes. In particular, we examine the pair distribution function, $g(r)$, the approaching relative velocities, $\langle \Delta v_n^-(r) \rangle$, and the collision kernel, $\kappa(r) = g(r)\langle \Delta v_n^-(r) \rangle$, as a function of the distance between the particle pairs. The laminar cases show the highest values of $\langle \Delta v_n^-(r) \rangle$ and $\kappa(r)$ while the turbulent flows assume lower values due to the homogeneity created by the turbulent eddies. The lowest values of $\langle \Delta v_n^-(r) \rangle$ and $\kappa(r)$ are found in the inertial shear-thickening regime, as a consequence of the particle packing in the core region. Separating the analysis in near-wall and centerline region, we observe larger values of $\langle \Delta v_n^-(r) \rangle$ and $\kappa(r)$ in the wall region due to the strongest background shear.

We have therefore demonstrated that the local particle dynamics clearly reflects the existence of the different flow regimes. The Bagnold number is shown to correctly predict the bulk flow behavior for the parameter range of this study; however, the details of the momentum transport and dissipation are different in the turbulent and particle-dominated regimes at low and high volume fraction, something which should be considered in any modeling effort. We believe future work should consider the role of the particle and fluid inertia and the particle dynamics in a mixture of particles of different sizes.

Acknowledgments

References

Bagnold, R., 1954. Experiments on a gravity-free dispersion of large solid spheres in a Newtonian fluid under shear. Proc. R. Soc. Lond. Ser. A. Math. Phys. Sci. 225, 49–63.

Balachandar, S., Eaton, J.K., 2010. Turbulent dispersed multiphase flow. Annu. Rev. Fluid Mech. 42, 111–133.

Batchelor, G.K., 1970. The stress system in a suspension of force-free particles. J. Fluid Mech. 41, 545–570.

Breedveld, V., Ende, D.V.D., Tripathi, A., Acrivos, A., 1998. The measurement of the shear-induced particle and fluid tracer diffusivities in concentrated suspensions by a novel method. J. Fluid Mech. 375, 297–318.

Breugem, W.-P., 2010. A combined soft-sphere collision/immersed boundary method for resolved simulations of particulate flows. In: Proceedings of the ASME 2010 3rd Joint US-European Fluids Engineering Summer Meeting and 8th International Conference on Nanochannels, Microchannels, and Minichannels, Montreal, Canada, vol. 21, p. 11.

Breugem, W.-P., 2012. A second-order accurate immersed boundary method for fully resolved simulations of particle-laden flows. J. Comput. Phys. 231, 4469–4498.

Brown, E., Jaeger, H., 2009. Dynamic jamming point for shear thickening suspensions. Phys. Rev. Lett. 103, 086001.

Campbell, C.S., 1990. Rapid granular flows. Annu. Rev. Fluid Mech. 22, 57–92.

Cherukat, P., McLaughlin, J., 1994. The inertial lift on a rigid sphere in a linear shear flow field near a flat wall. J. Fluid Mech. 263, 1–18.

Cokelet, G., 1999. Viscometric, in vitro and in vivo blood viscosity relationships: how are they related? Biorheology 36, 343–358.

Cunha, F.D., Hinch, E.J., 1996. Shear-induced dispersion in a dilute suspension of rough spheres. J. Fluid Mech. 309, 211–223.

de Motta, J., Estivalezes, J.-L., Climent, E., Vincent, S., 2012. Direct numerical simulation of particle turbulence interaction in forced turbulence. Turbulent and Interactions – Proceedings of the TI Conference, vol. 125. Springer, pp. 23–29.

Eckstein, E.C., Bailey, D.G., Shapiro, A.H., 1977. Self-diffusion of particles in shear flow of a suspension. J . Fluid Mech. 79, 191–208.

Fall, A., Lemaître, A., Bertrand, F., Bonn, D., Ovarlez, G., 2010. Shear thickening and migration in granular suspensions. Phys. Rev. Lett. 105, 268303.

Gualtieri, P., Picano, F., Casciola, C.M., 2009. Anisotropic clustering of inertial particles in homogeneous shear flow. J. Fluid Mech. 629, 25–39.

Gualtieri, P., Picano, F., Sardina, G., Casciola, C.M., 2012. Statistics of particle pair relative velocity in the homogeneous shear flow. Physica D 241, 245–250.

Guazzelli, E., Morris, J., 2011. A Physical Introduction to Suspension Dynamics. Cambridge University Press.

Haddadi, H., Morris, J.F., 2014. Microstructure and rheology of finite inertia neutrally buoyant suspensions. J. Fluid Mech. 749, 431–459.

Hampton, R., Mammoli, A., Graham, A., Tetlow, N., Altobelli, S., 1997. Migration of particles undergoing pressure-driven flow in a circular conduit. J. Rheol. 41, 621.

Hasimoto, H., 1959. On the periodic fundamental solutions of the Stokes equations and their application to viscous flow past a cubic array of spheres. J. Fluid Mech. 5, 317–328.

Henningson, D., Kim, J., 1991. On turbulent spots in plane Poiseuille flow. J. Fluid Mech. 228, 183–205.

Hunt, M.L., Zenit, R., Campbell, C.S., Brennen, C.E., 2002. Revisiting the 1954 suspension experiments of R. A. Bagnold. J. Fluid Mech. 452, 1–24.

Janoschek, F., 2013. Mesoscopic Simulation of Blood and General Suspensions in Flow. Eindhoven University of Technology (Ph.D. thesis).

Kulkarni, P., Morris, J., 2008a. Pair-sphere trajectories in finite-Reynolds-number shear flow. J. Fluid Mech. 596, 413–435.

Kulkarni, P., Morris, J., 2008b. Suspension properties at finite Reynolds number from simulated shear flow. Phys. Fluids 20, 040602.

Lambert, R., Picano, F., Breugem, W.P., Brandt, L., 2013. Active suspensions in thin films: nutrient uptake and swimmer motion. J. Fluid Mech. 733, 528–557.

Lashgari, I., Picano, F., Brandt, L., 2015. Transition and self-sustained turbulence in dilute suspensions of finite-size particles. Theor. Appl. Mech. Lett. 5, 121–125.

Lashgari, I., Picano, F., Breugem, W.-P., Brandt, L., 2014. Laminar, turbulent and inertial shear-thickening regimes in channel flow of neutrally buoyant particle suspensions. Phys. Rev. Lett. 113, 254502.

Loisel, V., Abbas, M., Masbernat, O., Climent, E., 2013. The effect of neutrally buoyant finite-size particles on channel flows in the laminar-turbulent transition regime. Phys. Fluids 25, 123304.

Marchioro, M., Tanksley, M., Prosperetti, A., 1999. Mixture pressure and stress in disperse two-phase flow. Int. J. Multiph. Flow 25, 1395–1429.

Matas, J.-P., Morris, J., Guazzelli, E., 2003. Transition to turbulence in particulate pipe flow. Phys. Rev. Lett. 90, 1.

Matas, J.-P., Morris, J., Guazzelli, E., 2004. Inertial migration of rigid spherical particles in Poiseuille flow. J. Fluid Mech. 515, 171–195.

McLaughlin, J., 1991. Inertial migration of a small sphere in linear shear flows. J. Fluid Mech. 224, 261–274.

McLaughlin, J., 1993. The lift on a small sphere in wall-bounded linear shear flows. J. Fluid Mech. 246, 249–265.

Morris, J., 2009. A review of microstructure in concentrated suspensions and its implications for rheology and bulk flow. Rheol. Acta 48, 909–923.

Nott, P.R., Brady, J.F., 1994. Pressure-driven flow of suspensions : simulation and theory. J. Fluid Mech. 275, 157–199.

Picano, F., Breugem, W.-P., Brandt, L., 2015. Turbulent channel flow of dense suspensions of neutrally-buoyant spheres. J. Fluid Mech. 764, 463–487.

Picano, F., Breugem, W.-P., Mitra, D., Brandt, L., 2013. Shear thickening in non-Brownian suspensions: an excluded volume effect. Phys. Rev. Lett. 111, 098302.

Pope, S., 2000. Turbulent Flows. Cambridge University Press.

Prosperetti, A., 2004. The average stress in incompressible disperse flow. Int. J. Multiph. Flow 30, 1011–1036.

Reade, W.C., Collins, L.R., 2000. Effect of preferential concentration on turbulent collision rates. Phys. Fluid. 12, 10.

Saffman, P.G., 1965. The lift on a small sphere in a slow shear flow. J. Fluid Mech. 22, 385–400.

Schonberg, J., Hinch, E.J., 1989. Inertial migration of a sphere in Poiseuille flow. J. Fluid Mech. 203, 517–524.

Segré, G., Silberberg, A., 1961. Radial particle displacements in Poiseuille flow of suspensions. Nature 189, 209–210.

Sierou, A., Brady, J.F., 2004. Shear-induced self-diffusion in non-colloidal suspensions. J. Fluid Mech. 506, 285–314.

Sundaram, S., Collins, L.R., 1997. Collision statistics in an isotropic particle-laden turbulent suspension. Part 1. Direct numerical simulations. J. Fluid Mech. 335, 75–109.

ten Cate, A., Nieuwstad, C.H., Derksen, J.J., Van den Akker, H.E.A., 2002. Particle imaging velocimetry experiments and lattice-Boltzmann simulations on a single sphere settling under gravity. Phys. Fluids 14, 4012.

Uhlmann, M., 2005. An immersed boundary method with direct forcing for simulation of particulate flow. J. Comput. Phys. 209, 448–476.

Yeo, K., Maxey, M., 2011. Numerical simulations of concentrated suspensions of monodisperse particles in a Poiseuille flow. J. Fluid Mech. 682, 491–518.

Yu, Z., Wu, T., Shao, X., Lin, J., 2013. Numerical studies of the effects of large neutrally buoyant particles on the flow instability and transition to turbulence in pipe flow. Phys. Fluids 25, 043305.

Zhang, Q., Prosperetti, A., 2010. Physics-based analysis of the hydrodynamic stress in a fluid-particle system. Phys. Fluids 22, 033306.